Bridge mode shape identification using moving vehicles at traffic speeds through non-parametric sparse matrix completion

5 authors, including:

Nima Shirzad-Ghaleroudkhani
University of Alberta
9 PUBLICATIONS **38** CITATIONS

SEE PROFILE

Farid Ghahari
University of California, Los Angeles
60 PUBLICATIONS **645** CITATIONS

SEE PROFILE

Ertugrul Taciroglu
University of California, Los Angeles
227 PUBLICATIONS **2,422** CITATIONS

SEE PROFILE

Some of the authors of this publication are also working on these related projects:

Project — Special Collection of ASCE's Journal of Structural Engineering on "Advances in Data-Driven Risk-Based Performance Assessment of Structures and Infrastructure Systems"
View project

Project — Digital Twins for Bridge Health Monitoring & Management View project

Bridge Mode Shape Identification using Moving Vehicles at Traffic Speeds through Non-parametric Sparse Matrix Completion

[1]Qipei Mei, [1]Nima Shirzad-Ghaleroudkhani, [2]Mustafa Gül, [3]S. Farid Ghahari and [4]Ertugrul Taciroglu

[1] Ph.D. Student, Dept. of Civil & Env. Engineering, University of Alberta, Edmonton, AB, Canada

[2]Associate Professor (Corresponding Author: mustafa.gul@ualberta.ca), Dept. of Civil & Env. Engineering, University of Alberta, Edmonton, AB, Canada

[3]Assistant Project Scientist, Dept. of Civil & Env. Eng., University of California, Los Angeles, CA, USA

[4]Professor, Dept. of Civil & Env. Eng., University of California, Los Angeles, CA, USA

Abstract: Advances in smart infrastructure produces a natural demand of system identification techniques for structural health and performance monitoring that can be scaled to regions and large asset inventories. Conventional approaches require sensors to be installed, often in long-term deployments, on the monitored infrastructure systems, which is a costly undertaking when thousands of systems (e.g., bridges) need to be monitored. This paper presents a novel mode shape identification method for bridges that uses data collected from moving vehicles as input—a paradigm that can overcome limitations associated with conventional approaches. The method consists of two steps. First, the data collected from moving measurement points are mapped to virtual fixed points to generate a sparse matrix. Then, a "soft-imputing" technique is employed to fill the sparse matrix. Finally, a singular value decomposition is applied to extract the mode shapes of the bridge. Experiments with synthetic, yet realistic, data are conducted to verify the method. The sensitivity of the proposed approach to different factors, including the number of vehicles, car speed, road roughness, and measurement errors are also investigated. The results show that the proposed method is capable of identifying the mode shapes of the bridge accurately.

Keywords: mobile sensing; moving vehicle; mode shape identification; matrix completion; soft-imputing

Nomenclature

Table 1 – List of symbols and notations in this paper

Symbol	Description
m	The number of moving measurement points (MMPs)
n	The number of virtual fixed points (VFPs)
t	Time step
V	Velocity of the MMPs
$x_i(t)$	The location of the ith MMP relative to the left end of the bridge at time step t
s_i	The location of the ith VFP relative to the left end of the bridge
$y(x, t)$	The vertical displacement of the bridge at location x and time t
$\phi_k(x)$	The kth mode shape at location x
$q_k(t)$	The generalized coordinate for the kth mode
$\mathbf{Y}(t)$	The displacement vector for all MMPs at time t
$\mathbf{Q}(t)$	The generalized coordinate vector for all modes at time t
$\mathbf{\Phi}(t)$	The shape function at the locations of MMPs at time t
$\mathbf{L}(t)$	The mapping function converting the displacement from MMPs to VFPs
$\mathbf{\Phi}^s$	The shape function at the locations of all VFPs
$\mathbf{D}$	The matrix constructed from the displacement vectors and mapping functions with missing values
$\mathbf{Z}$	The estimated matrix according to $\mathbf{D}$
$\mathbf{Z_{old}}$	The estimated matrix according to $\mathbf{D}$ before an iteration
$\mathbf{Z_{new}}$	The estimated matrix according to $\mathbf{D}$ after an iteration
λ_i	The ith regularization coefficient
$\mathbf{\Omega}$	The set including the indices of all valid data
$\|\cdot\|_n$	The nuclear norm of a matrix
$\|\cdot\|_*$	The rank of a matrix
$\mathbf{P_\Omega(D)}$	A new constructed matrix that keeps the values of all the valid data in matrix D and set all the missing data of D to zero.
$\mathbf{P_\Omega^\perp(D)}$	Complementary projection of $\mathbf{P_\Omega(D)}$ where $\mathbf{P_\Omega(D)} + \mathbf{P_\Omega^\perp(D)} = \mathbf{D}$

1. Introduction

The term "Smart city" refers to a city where networked sensors and computational algorithms that make use of data from sensors are employed for improving the efficiency of infrastructure components, often towards goals involving resiliency and sustainability. [1-3] With massive growth in urban population, resiliency and sustainability of urban centers have become highly dependent with their transportation infrastructure. [4-7] Many studies show that any disruption in the performance of bridges, which are key components of developed transportation networks, could result in irreversible economic and social losses. [8-10] This vulnerability is, in fact, more acute in many developed countries, because a substantial portion of their bridge stock have reached their design life, and their serviceability relies on a regular monitoring and maintenance operations. For instance, Canadian Infrastructural Report Card [11] assessed about 26% of bridges in Canada to be in fair, poor, or very poor conditions, which are under the risk of further deterioration. The situation in the United States is very similar. [12] Naturally, bridge condition assessment methodologies have garnered increasing interest in recent years. [13-15]

First step of bridge condition assessment is data collection. Most conventional methods rely on fixed sensors to collect data from bridges (see, e.g., [16-22]). The efficiency and performance of these methods have been examined and demonstrated in those studies. However, these methods require each bridge to be instrumented with fixed sensors, which is costly, time-consuming, and, at the present time, almost impractical to be applied to a large number of bridges. As such, new "mobile sensing" technologies have recently been considered for bridges that use data collected from instrumented traversing vehicles. [23] This technology eliminates the need to install fixed sensors on bridges, which brings forth the possibility to monitor a large number of bridges through the use of instrumented vehicles.

The concept of capturing the information of the bridge using a sensor installed in a moving vehicle was first proposed by Yang et al. [24] The challenge of this concept lies in the fact that the data measured on the moving vehicle include coupled information from both the vehicle and the bridge. Different techniques have to be applied to the recorded mixed responses in order to extract the dynamic characteristics of the bridge. [25-29] In Yang et al. [24], the dynamic analysis of vehicle-bridge interaction was performed for an analytical bridge-vehicle system, consisting of a simple 2D beam representing the bridge, and a moving mass-spring system representing the vehicle. It was shown that the bridge frequency could be extracted from the vibration of the vehicle. Subsequently, a number of studies followed up on the notion of mobile sensing through analytical/numerical analyses [30-34], as well as laboratory-scale [28, 35-40], and real-life experiments [19, 41].

One way to assess the condition of a bridge through mobile sensing is based on modal characteristics. In this class of methods, the data collected from moving vehicles are used to estimate the frequencies and mode shapes of the bridge, which then can be used for further assessment of the bridge condition. The accuracy of mode shape identification is key to properly assess the condition of the bridge. In this particular thread of work, Oshima et al. [42] proposed a method to detect support damages based on the mode shapes identified after mapping the moving sensor data to fixed sensors. In another study, Malekjafarian and O'Brien [43] presented an algorithm for bridge damage detection

based on the mode shapes obtained using the Short Time Frequency Domain Decomposition (STFDD) method. Later on in OBrien and Malekjafarian [44], they improved their method using laser vibrometers and accelerometers to achieve high resolution mode shapes. Empirical Mode Decomposition (EMD)—a well-known modal identification method—was investigated in another study. [45] Matarazzo et al. [27] introduced a method dubbed "structural identification using expectation maximization (STRIDE)" for mode shape identification from mobile sensors. Their method consisted of two steps, where the first (expectation) step was to update the missing observations due to mobile sensing, and the second (maximization) step was to update the parameters of the state-space representation of the system. Hilbert Transform was also shown to be an effective technique in identifying bridge mode shapes. [25, 46] Yang et al. [46] found that the instantaneous amplitude of the vehicle includes mode shape information, and developed a method based on Hilbert transform to reconstruct the mode shapes from measured responses of the moving vehicle. In that study, they identified the vehicle speed, random traffic and road roughness as important factors affecting the accuracy of their method. Malekjafarian and Obrien [25] related the energy calculated from Hilbert Huang Transform (HHT) to the mode shapes. Using the data collected from two adjacent axles of a vehicle and empirical mode decomposition, the first mode shape was reconstructed. One limitation of the aforementioned two studies was that engineering judgement had to be applied to determine the signs of the mode shapes. Eshkevari et al. [47-49] treated the mobile sensing data as a sparse matrix with missing values. In their work, alternating least-square (ALS) was used to complete the matrix. Then, system identification techniques such as principal component analysis (PCA) and structured optimization analysis (SOA) are used to identify modal properties.

As identified in several prior studies [23, 25, 43], the challenges of mode shape identification using moving vehicles mainly include the following: (*i*) the accuracy of mode shape identification is adversely affected by the limited vehicle bridge interaction time, as indicated in Malekjafarian and Obrien; [25] (*ii*) Since the sensor usually stays in one location for a very short period, high accuracy in mode shape identification is only achievable by carefully accounting for vehicle-bridge interaction, and by using multiple mobile sensors. [27]

In recent years, matrix completion methods have gained much attention from researchers in structural health monitoring. One major advantage of matrix completion methods is that they are fully data-driven, which does not require prior knowledge about the bridges. They have been successfully applied to system identification of bridges using either fixed sensors [50] or mobile sensors [34, 48, 49]. Yang and Nagarajaiah [50] investigated two methods to recover the randomly missing values in structural vibration responses. One was based on $\ell 1$-minimization, and the other was based on nuclear norm minimization. The effectiveness and efficiency of the methods were compared on the real-life data about the Canton Tower and a cable-stayed bridge. More detailed review about system identification of structures using matrix completion methods can be found in Nagarajaiah and Yang [51]. Eshkevari et al. [34, 48, 49] treated the mobile sensing data as a sparse matrix with missing values. In their work, alternating least-square (ALS) was used to complete the matrix. Then, system identification techniques such as principal component analysis (PCA) and structured optimization analysis (SOA) were used to identify modal properties.

This paper proposes a new method for mode shape identification from moving vehicles by converting the problem into a matrix completion problem, and through a mapping process and implementing a "soft imputing" algorithm proposed by Mazumder et al.[52] to iteratively fill/complete the matrix. There are several advantages of the proposed method with respect to previousmethods: (*i*) Since the method does not explicitly use frequency domain information for system identification, it can work at traffic speeds with limited vehicle-bridge-interaction time. (*ii*) Owing to the mapping step in the method, the method can achieve high accuracy with a limited number of sensors. (*iii*) Since the soft imputing algorithm is non-parametric, no information about the dynamic system is required.

The remainder of this manuscript is organized as follows: First, the methodology proposed in this study is introduced in §2. Then, numerical analyses are conducted in §3 to verify the method. The characteristics of the proposed method are discussed in §4, and conclusions, limitations, and recommended future work are provided in §5.

2. Methodology

2.1. Assumptions

In the present study, the sensors are assumed to be placed on the front and rear axles of the vehicle (see Figure 1) to mitigate the influence of the suspension system. The deformation of the wheels and tires are ignored for simplicity. In practice, the effect of the vehicle's dynamic system can be removed, for example, by using its empirical transfer function. It is assumed that recorded data are accelerations, which are integrated twice to obtain the displacements, and serve as inputs to the matrix completion algorithm. The weight of the vehicles is assumed to be negligible compared to the weight of the bridge to ensure a linear time invariant system. The speeds of traversing vehicles are assumed to be the identical, and constant. It is noted that the speed assumptions are made for simplicity, and the method devised in the present study can be generalized in a straightforward manner. The list of symbols and notations used in this paper is provided in Table 1.
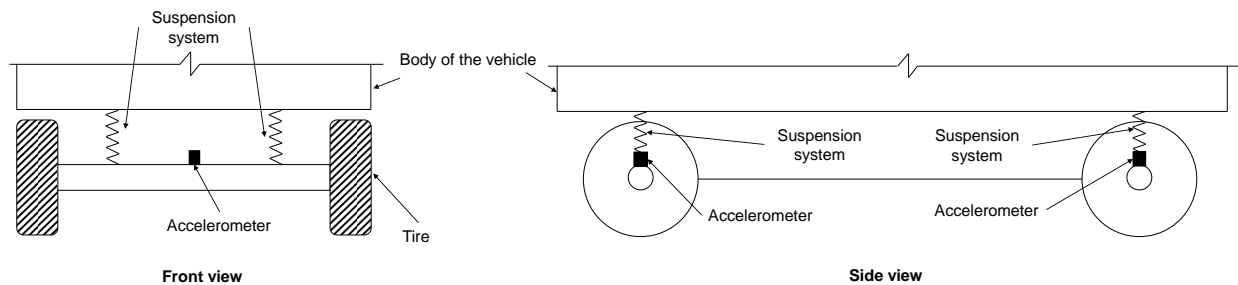

Figure 1 – illustration of the sensor installation

2.2. Mapping moving observations to fixed observations

Two terms are defined first—namely, moving measurement point (MMP), and virtual fixed points (VFP). Each MMP represents a mobile sensor on the moving vehicle; and each VFP is a virtual sensor placed at a fixed location. There is no direct measurement at VFPs. As shown in Figure 2, in the

proposed method, the observations from MMPs are first mapped to the virtual fixed points VFPs using linear interpolation.
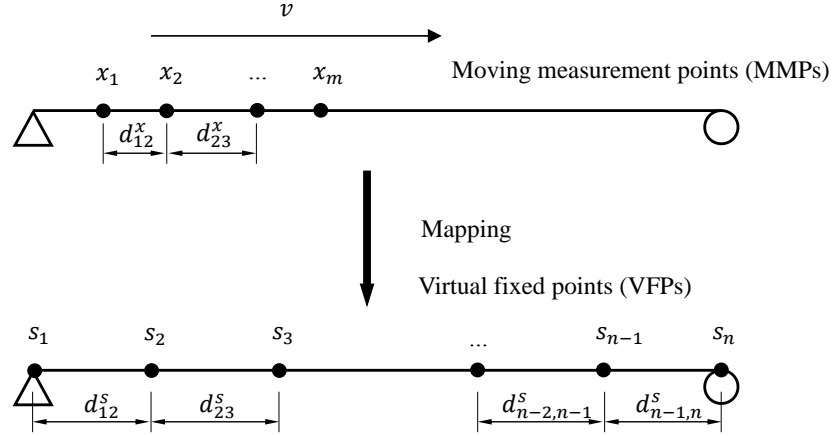

Figure 2 – Mapping moving measurement points to fixed points

Considering the modal superposition, the vertical displacement $y(x_i(t),t)$ of the ith MMP can be expressed as

$$y(x_i(t),t) = \sum_{k=1}^{n_d} \phi_k(x_i(t))q_k(t) \tag{1}$$

where $\phi_k(x_i(t))$ is the value of kth mode shape at location $x_i(t)$, and $q_k(t)$ is the generalized coordinate for k^{th} mode. The Eq. (1) can be written in a matrix form by applying to all MMPs, as seen in Eqs. (2) and (3) below.

$$\begin{pmatrix} y(x_1(t),t) \\ y(x_2(t),t) \\ \vdots \\ y(x_m(t),t) \end{pmatrix} = \begin{bmatrix} \phi_1(x_1(t)) & \phi_2(x_1(t)) & \cdots & \phi_{n_d}(x_1(t)) \\ \phi_1(x_2(t)) & \phi_2(x_2(t)) & \cdots & \phi_{n_d}(x_2(t)) \\ \vdots & \vdots & \ddots & \vdots \\ \phi_1(x_m(t)) & \phi_2(x_m(t)) & \cdots & \phi_{n_d}(x_m(t)) \end{bmatrix} \begin{pmatrix} q_1(t) \\ q_2(t) \\ \vdots \\ q_{n_d}(t) \end{pmatrix} \tag{2}$$

$$\mathbf{Y}(t) = \mathbf{\Phi}(t)\mathbf{Q}(t) \tag{3}$$

In the equation above, $\mathbf{Y}(t)$ represents the displacement vector for all MMPs, $\mathbf{Q}(t)$ is the generalized coordinates for all modes at time t, and $\mathbf{\Phi}(t)$ is the shape function at the location of MMPs at time t. It should be noted that $\mathbf{\Phi}(t)$ is not the mode shape matrix of the bridge since it is dependent on the time.

To obtain the mode shape, the shape function value at location x can be projected to n base functions through Eq. (4), where n is the number of VFPs.

$$\phi_k(x) = \sum_{j=1}^{n} a_{jk}l_j(x) \tag{4}$$

The proposed $l_j(x)$ is given in Eq. (5). Unlike in [42], this study uses linear interpolation from adjacent fixed points instead of all the points because the interpolation using all VFPs has a very high order, which can result in a large error when being inversed.

$$l_j(x) = \begin{cases} \dfrac{x - s_{j-1}}{s_j - s_{j-1}} & s_{j-1} \leq x \leq s_j \\ \dfrac{x - s_{j+1}}{s_j - s_{j+1}} & s_j < x \leq s_{j+1} \\ 0 & \text{otherwise} \end{cases} \tag{5}$$

Substituting the location of one VFP, s_p, into Eq. (4) results in the following equation,

$$\phi_k(s_p) = \sum_{j=1}^{n} a_{jk} l_j(s_p) = a_{pk} \frac{s_p - s_{p-1}}{s_p - s_{p-1}} = a_{pk} \tag{6}$$

Therefore, Eq. (4) can be written as in Eq. (7) for the location of MMP i,

$$\phi_l(x_i(t)) = \sum_{j=1}^{n} \phi_k(s_j) l_j(x_i(t)) \tag{7}$$

Writing Eq. (7) in matrix form for all modes, the Eqs. (8) and (9) can be obtained as follows,

$$
\begin{bmatrix}
\phi_1(x_1(t)) & \phi_2(x_1(t)) & \cdots & \phi_{n_d}(x_1(t)) \\
\phi_1(x_2(t)) & \phi_2(x_2(t)) & \cdots & \phi_{n_d}(x_2(t)) \\
\vdots & \vdots & \ddots & \vdots \\
\phi_1(x_m(t)) & \phi_2(x_m(t)) & \cdots & \phi_{n_d}(x_m(t))
\end{bmatrix}
=
\begin{bmatrix}
l_1(x_1(t)) & l_2(x_1(t)) & \cdots & l_n(x_1(t)) \\
l_1(x_2(t)) & l_2(x_2(t)) & \cdots & l_n(x_2(t)) \\
\vdots & \vdots & \ddots & \vdots \\
l_1(x_m(t)) & l_n(x_m(t)) & \cdots & l_n(x_m(t))
\end{bmatrix}
$$

$$
\times
\begin{bmatrix}
\phi_1(s_1) & \phi_2(s_1) & \cdots & \phi_{n_d}(s_1) \\
\phi_1(s_2) & \phi_2(s_2) & \cdots & \phi_{n_d}(s_2) \\
\vdots & \vdots & \ddots & \vdots \\
\phi_1(s_n) & \phi_2(s_n) & \cdots & \phi_{n_d}(s_n)
\end{bmatrix}
\tag{8}
$$

$$\mathbf{\Phi}(t) = \mathbf{L}(t)\mathbf{\Phi}^s \tag{9}$$

In Eq. (9), the right side is the multiplication of two matrices. The first one, $\mathbf{L}(t)$, is the mapping function converting the displacement from MMPs to VFPs, and the second one is the shape function at n VFPs. The second matrix will not change with time and is the mode shape of the bridge. Substituting Eq. (9) into Eq. (3) yields to the following relationship,

$$\mathbf{Y}(t) = \mathbf{\Phi}(t)\mathbf{Q}(t) = \mathbf{L}(t)\mathbf{\Phi}^s\mathbf{Q}(t) \tag{10}$$

Multiplying Eq. (10) by the inverse of $\mathbf{L}(t)$ produces

$$\mathbf{L}^{-1}(t)\mathbf{Y}(t) = \mathbf{\Phi}^s \mathbf{Q}(t) \tag{11}$$

It should be noted here that if $m \neq n$, i.e. $\mathbf{L}(t)$ is not a square matrix, then the pseudoinverse should be evaluated instead of the inverse. $\mathbf{L}^{-1}(t)\mathbf{Y}(t)$ is a vector with n elements, and the following matrix $\mathbf{D}$ in Eq. (12) is defined with columns representing time steps, where K is the total number of time steps, and rows representing VFPs.

$$\mathbf{D} = \begin{bmatrix} \mathbf{L}^{-1}(t_1)\mathbf{Y}(t_1) & \mathbf{L}^{-1}(t_2)\mathbf{Y}(t_2) & \cdots & \mathbf{L}^{-1}(t_K)\mathbf{Y}(t_K) \end{bmatrix} = \mathbf{\Phi}^s \begin{bmatrix} \mathbf{Q}(t_1) & \mathbf{Q}(t_2) & \cdots & \mathbf{Q}(t_K) \end{bmatrix} \tag{12}$$

In practice, the displacement is difficult to measure. Therefore, in this study, the acceleration data is numerically integrated twice to obtain the displacement.

2.3. Valid data points

Even though the inverse of the mapping function matrix $\mathbf{L}(t)$ is applied to all MMPs and VFPs, we observe the errors between the converted displacements at VFPs and the ground truth are small only when there are at least two MMPs in the region formed by two VFPs adjacent to the given VFP. We define the mapping within this range as valid and consider the other elements as invalid or missing. An example with 4 MMPs is presented in Figure 3. At certain time t, there are two MMPs between VFPs, s_2 and s_3, so these two VFPs have valid data at time t. Since all other VFPs do not have at least two MMPs in their adjacent segments, data for these VFPs are invalid and are considered as missing. The reason behind requiring at least two MMPs is that the linear interpolation is used to represent the displacement at an MMP using two VFPs. At least two MMPs are required to fully determine the inverse function of the mapping.
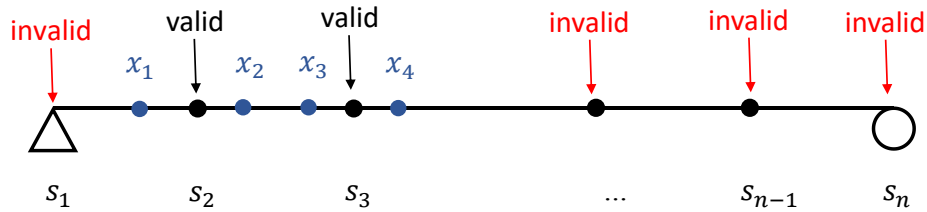

Figure 3 – Illustration of the valid and invalid data points

Since the invalid data cannot be used for system identification, the matrix $\mathbf{D}$ will have many missing values. A typical matrix $\mathbf{D}$ is presented in Figure 4 for visualization purpose. Figure 4 illustrates that as the time goes on and the MMPs move to the right, VFPs at the right side start to get valid data.
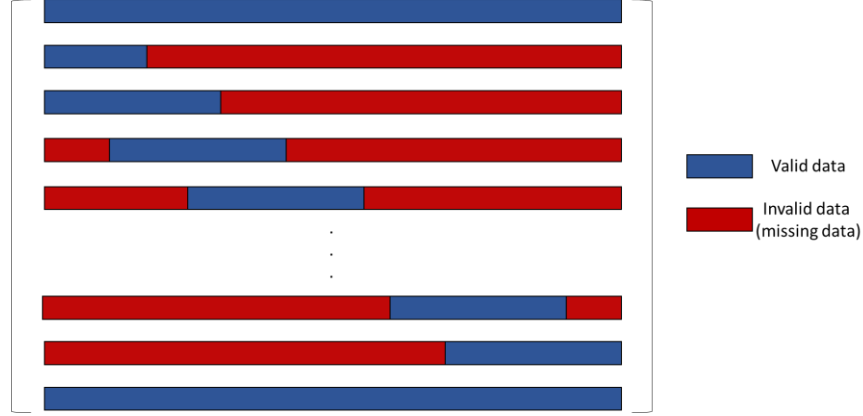
Figure 4 – Visualization of a typical **D** matrix

2.4. Matrix Completion using Soft Imputing

System identification techniques cannot be directly applied to the matrix with missing values. To overcome this issue, a technique called soft imputing is applied to look for patterns in the data and fill the matrix using an expectation maximization framework. The reason we choose soft imputing algorithm for matrix completion is that there is no need to assume the rank of the estimated matrix. Also, the Singular Value Decomposition (SVD) within this algorithm can guarantee the orthogonality of the factorized matrices, which is a property of mode shapes. This algorithm has a time complexity of O(n) which is also efficient in implementation. [52, 53]

In this framework, the missing data are assumed and updated in an iterative process. Consider a matrix $\mathbf{P}_\Omega(\mathbf{D})$ with element defined as below,

$$\mathbf{P}_\Omega(\mathbf{D})(i,j) = \begin{cases} \mathbf{D}(i,j) & (i,j) \in \Omega \\ 0 & (i,j) \notin \Omega \end{cases} \tag{13}$$

where Ω is the set including the indices of all valid data. This matrix keeps the values of all the valid data and set all the missing data to zero. Similarly, $\mathbf{P}_\Omega^\perp(\mathbf{D})$ is defined as complementary projection of $\mathbf{P}_\Omega(\mathbf{D})$ where $\mathbf{P}_\Omega(\mathbf{D})+\mathbf{P}_\Omega^\perp(\mathbf{D})=\mathbf{D}$.

Assuming the estimated matrix is **Z,** all the elements in **Z** are valid. There are two objectives for the optimization algorithm to fill the matrix **D**. First, $\mathbf{P}_\Omega(\mathbf{Z})$ as defined as elements in **Z** corresponding to the valid elements in **D** should be as close to $\mathbf{P}_\Omega(\mathbf{D})$ as possible. Second, the rank of the estimated matrix **Z** should be as low as possible. This is a regularization term based on the assumption that using fewer modes to represent the vibration is expected to be more accurate than using more modes. According to the descriptions above, the following objective function is defined,

$$\underset{z}{\text{minimize}} \quad f_\lambda(\mathbf{Z}) = \frac{1}{2}\left\|\mathbf{P}_\Omega(\mathbf{D}) - \mathbf{P}_\Omega(\mathbf{Z})\right\|_n^2 + \lambda_i \times \left\|\mathbf{Z}\right\|_* \tag{14}$$
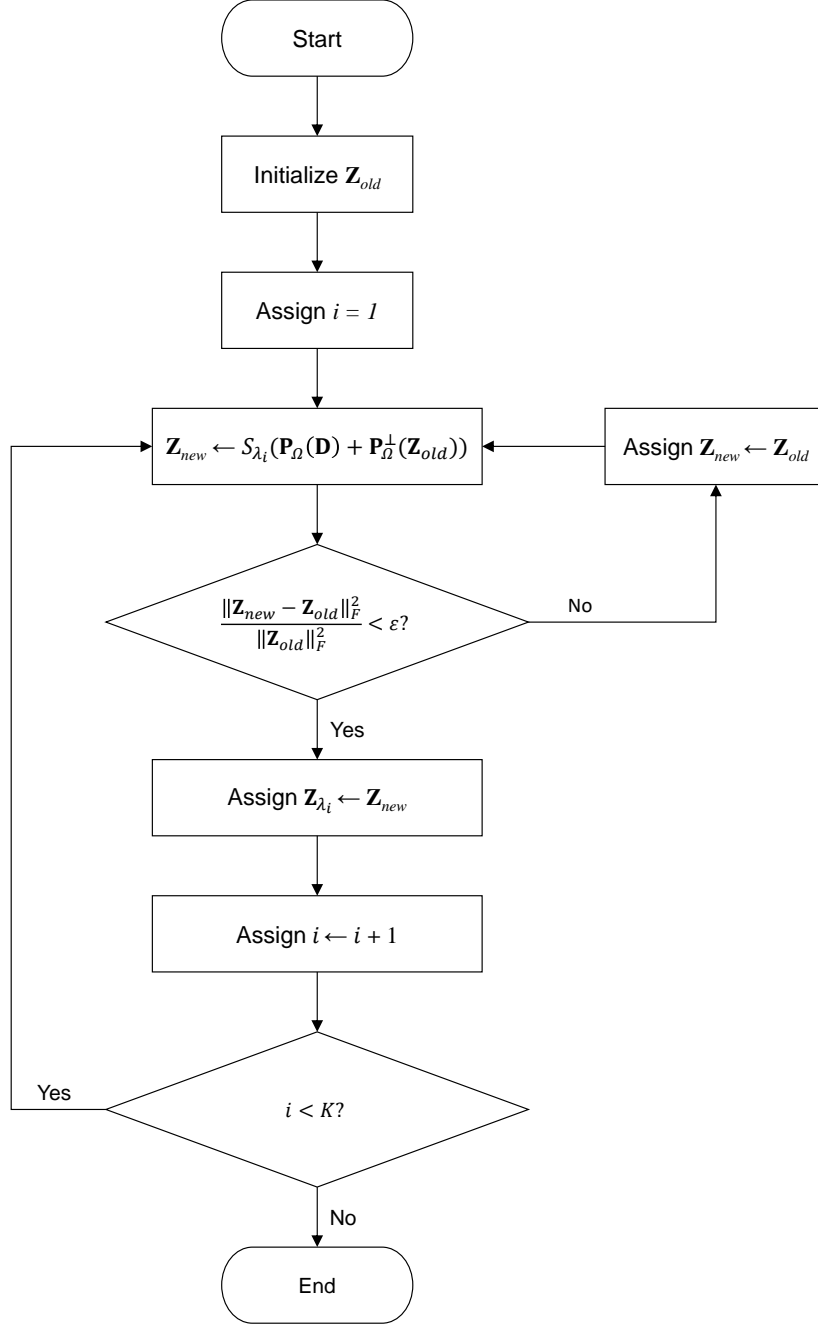
Figure 5 – Soft imputing algorithm for matrix completion

where $\|\cdot\|_n$ represents the nuclear norm of a matrix and $\|\cdot\|_*$ is the rank of the matrix. λ_i is the regularization coefficient, which plays an important role in the algorithm. This optimization problem can be solved iteratively, as presented in Figure 5. At the beginning, the $\mathbf{P_\Omega}(\mathbf{Z}_{\text{old}})$ is set to $\mathbf{P_\Omega}(\mathbf{D})$, and $\mathbf{P_\Omega^\perp}(\mathbf{Z}_{\text{old}})$ is initialized randomly. λ_i are chosen in a descending order, and λ_1 should be smaller than the maximum singular value of $\mathbf{Z}_{\text{old}}$. As stated in Oshima et al. [52], for a given λ_i, the solution $\mathbf{Z}_{new}$ for the above optimization problem is given by the following iterative process.

$$\mathbf{Z}_{new} = S_{\lambda_i}(\mathbf{P_\Omega}(\mathbf{D}) + \mathbf{P_\Omega^\perp}(\mathbf{Z}_{old})) = \mathbf{U}\mathbf{\Sigma}_{\lambda_i}\mathbf{V}$$

$$\mathbf{\Sigma}_{\lambda_i} = \text{diag}[(d_1 - \lambda_i)_+, (d_2 - \lambda_i)_+, \cdots, (d_r - \lambda_i)_+], r = \min(m, n)$$

(15)

where $\mathbf{U}$, $\mathbf{\Sigma}$, $\mathbf{V}$ are determined by Singular Value Decomposition (SVD) of a new matrix $\mathbf{P_\Omega}(\mathbf{D}) + \mathbf{P_\Omega^\perp}(\mathbf{Z}_{old})$, and specifically $\mathbf{\Sigma} = \text{diag}(d_1, d_2, \cdots d_r)$ consists of the singular values. The matrix $\mathbf{\Sigma}_{\lambda_i}$ is the soft-thresholded matrix of $\mathbf{\Sigma}$, in which the notation $(\cdot)_+$ means the larger of the given value and 0 for each element. Repeating the process of replacing the missing value with the current guess and updating through Eq. (15), the matrix can be imputed after converging. As shown in Figure 5, the algorithm will generate a series of $\mathbf{Z}_{\lambda_i}$, and the optimal one determined by the objective function value, i.e. Eq. (14), as well as engineering judgement, can be used for further analysis. The optimal Z_{λ_i} is termed as $\mathbf{Z}_{opt}$.

2.5. System Identification

After obtaining the optimal estimated matrix $\mathbf{Z}_{opt}$, different system identification techniques can be applied to retrieve the mode shapes of the bridge. In this study, SVD is used as it reserves the orthogonality of mode shapes in the decomposition. The estimated matrix $\mathbf{Z}_{opt}$ has the same dimension as the matrix $\mathbf{D}$ which is $n \times K$. The SVD of $\mathbf{Z}_{opt}$ can be expressed as,

$$\mathbf{Z}_{opt} = \mathbf{U}_{opt}\mathbf{\Sigma}_{opt}\mathbf{V}_{opt}^T$$

(16)

Comparing Eq. (16) with Eq. (11), it is inferred that $\mathbf{U}_{opt}$ relates to the mode shapes of the bridge since they are both orthogonal. By normalizing the $\mathbf{U}_{opt}$, the mode shape of the bridge will be extracted.

3. Numerical Verification

3.1. Numerical Setup

To verify the proposed method, numerical analyses are conducted using ABAQUS on a simply supported bridge, as illustrated in Figure 6. The length of the bridge is 40 m. The rectangular cross section of the bridge has a width of 3 m and a height of 1.5 m. The bridge is made of concrete, which has a density of 2400 kg/m^3 and elastic modulus of 27.5 GPa. The first three frequencies of the bridge are 1.44 Hz, 5.76 Hz and 12.95 Hz. Two MMPs are placed on the bridge with a distance of 2.5 m to represent the wheels of a single vehicle. A constant speed of 40 km/h is assigned to all the MMPs, and the linear implicit dynamic analysis is conducted with contacts among MMPs and the bridge. Therefore, the analysis ends when the foremost MMP reaches the right end of the bridge. The sampling frequency of acceleration is 200 Hz.
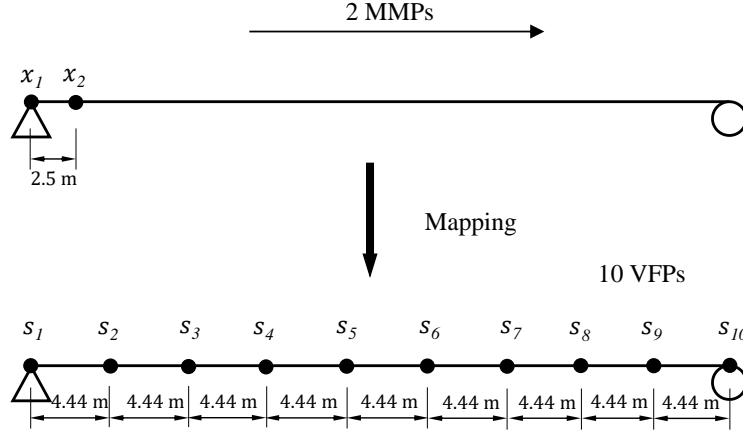
Figure 6 – Setup of the numerical analysis

3.2. Results and Analysis

Figure 7 presents the measured accelerations, integrated velocities, and integrated displacements for 2 MMPs. As described in §2, acceleration is considered as the measurement from the analysis. In this study, trapezoidal numerical integrations are applied twice to obtain the displacements, which are the input to the mapping and matrix completion procedures. In Figure 7, it is seen that the integrated displacements are not stationary. They follow the pattern of the deflection of a simply supported bridge where the absolute displacement is the highest near mid-span, but they are in a vibration form due to the moving of the vehicle.
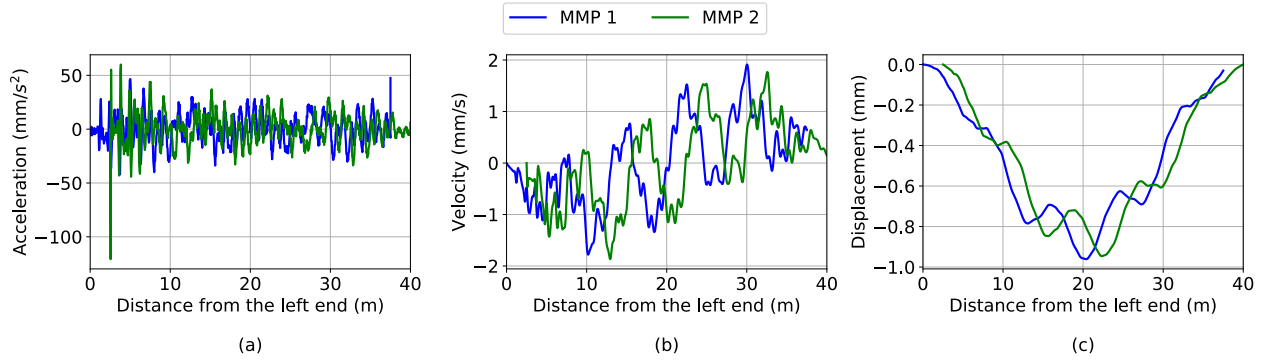

Figure 7 - Measured acceleration and integrated velocity and displacement for 2 MMPs: (a) measured acceleration; (b) integrated velocity; (c) integrated displacement

The integrated displacements are then mapped to 10 VFPs in order to construct displacements at those VFPs following the procedure described in section 2.2. As mentioned earlier, it is assumed that the mapping is only valid when there are more than two MMPs in a VFP's adjacent segments, as demonstrated in Figure 3. The invalid data in the matrix $\mathbf{D}$ are considered as missing data. Then, the matrix completion algorithm described in section 2.4 is applied to fill these missing values. The maximum singular value of the initialized $\mathbf{Z}$ is 0.02. A series of 11 λ values are given in descending order to the algorithm. λ values chosen are 1×10^{-2}, 5×10^{-3}, 1×10^{-3}, 5×10^{-4}, 1×10^{-4} 5×10^{-5}, 1×10^{-5}, 5×10^{-6}, 1×10^{-6}, 5×10^{-7} and 1×10^{-7}, respectively. The threshold $\mathcal{E}$ is set to 1×10^{-15}, and the maximum number of iterations for each λ is 10^5. The optimal λ is determined by measuring the error between

valid elements within estimated matrix $\mathbf{Z}$ and matrix $\mathbf{D}$ and using engineering judgement. The optimal λ will be used to generate final output for further analysis.

Figure 8 compares the estimated $\mathbf{Z}$ matrix obtained by completing matrix $\mathbf{D}$ with ground truth displacements extracted at VFPs. Four out of ten VFPs are chosen for better visualization. In Figure 8 (a), the solid portions of the curves are measured valid displacements mapped from the MMPs, and the dotted portions of the curves are estimated from the proposed algorithms. Figure 9 shows the errors relative to the amplitude of that specific VFP (minimum absolute displacement). It should be noted that even the measured data (solid portions of the curves) are not exactly equal to the ground truth, shown in Figure 8 (b), due to the mapping process. This phenomenon could be explained by Figure 10. The valid points are defined when there are more than 2 MMPs in a VFP's adjacent segments. When only 2 MMPs are used, there is a chance that 2 MMPs cross the valid points, i.e. s_i in Figure 10. In this case, taking the pseudoinverse is equivalent to calculating values at three VFPs, i.e. s_{i-1}, s_i, and s_{i+1}, from two MMPs even though only data from one VFP, i.e. s_i, is considered as valid. This problem is underdetermined, and the mapping could cause errors. In following sections, it will be shown that when more MMPs are used, these errors can be reduced.

(a) Matrix Z obtained by completing D   (b) Ground truth
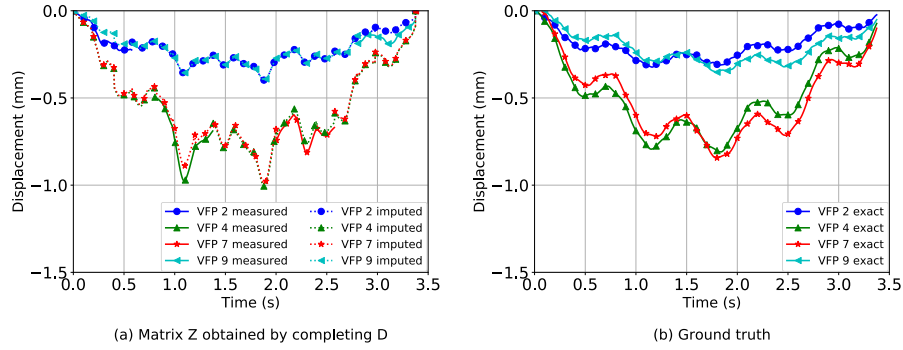
Figure 8 - Comparison between reconstructed displacements for 4 VFPs and ground truth (2 MMPs)
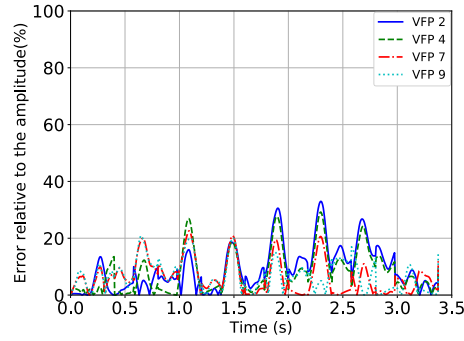

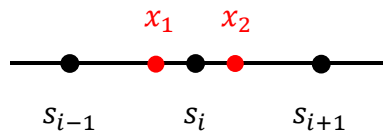Figure 9 – Errors relative to the amplitude of each VFP (2 MMPs)

Figure 10 - Mapping from 2 MMPs

Following the mapping process, the matrix completion algorithm is implemented to find the internal relationship of displacements at different VFPs and to use this relationship to complete the matrix $\mathbf{D}$. The matrix completion process is non-parametric which means no physical model is required for the process. The matrix $\mathbf{D}$ has a dimension of 10×677 with 4496 missing values. The missing rate for matrix $\mathbf{D}$ is 66.41%. It should be noted that the matrix $\mathbf{D}$ is constructed by mapping from 2 MMPs (2×677).

After obtaining the matrix $\mathbf{Z}$, i.e. completed from of matrix $\mathbf{D}$, SVD is applied to extract the mode shapes of the bridge. The identified mode shapes are summarized in Figure 11. In order to quantitatively measure the similarity between the identified and the exact mode shapes, the Modal Assurance Criterion (MAC) is calculated using Eq. (17),

$$\mathrm{MAC}(\phi_{\mathrm{identified}}, \phi_{\mathrm{exact}}) = \frac{\left(\phi_{\mathrm{identified}}^T \phi_{\mathrm{exact}}\right)^2}{\left(\phi_{\mathrm{identified}}^T \phi_{\mathrm{identified}}\right)\left(\phi_{\mathrm{exact}}^T \phi_{\mathrm{exact}}\right)} \tag{17}$$

where $\phi_{\mathrm{identified}}$ and ϕ_{exact} are the vectors representing the identified and the exact mode shapes. The MAC values for these modes are 1.000, 0.998 and 0.977. It is seen that the system identification is very accurate even though the mapping is not exact.
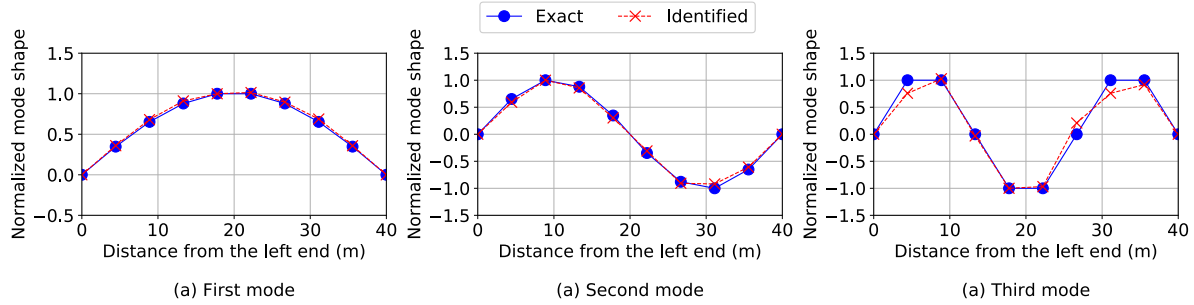

Figure 11 - The first three normalized mode shapes identified using 2 MMPs

4. Discussion

4.1. Influence of the number of MMPs

As described before, in this study, two MMPs represent a car, and the number of cars is expected to have effect on the mode shape identification. In this section, the effect of the number of MMPs on the identification results is investigated. Figure 12 presents the displacement values integrated from acceleration data for 4, 6 and 8 MMPs. As seen, the displacements for different numbers of MMPs have similar patterns, but the maximum displacement is larger when more MMPs are on the bridge.
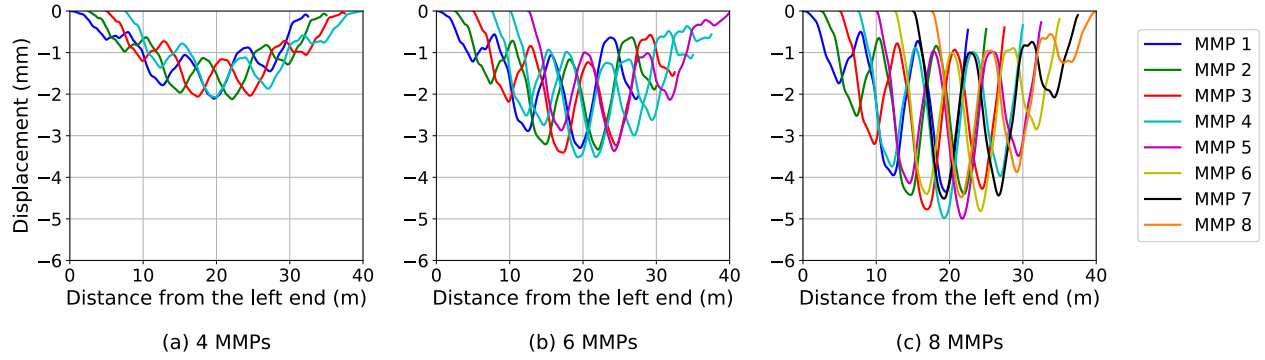
(a) 4 MMPs (b) 6 MMPs (c) 8 MMPs

Figure 12 - Integrated displacement for 4, 6 and 8 MMPs

Similar to Figure 8 in the previous section, Figure 13, Figure 14, and Figure 15 show comparisons between the matrix $\mathbf{Z}$ after completing matrix $\mathbf{D}$ and ground truth displacements at VFPs for different number of MMPs. We can see in Figure 13(a), Figure 14(a), and Figure 15(a), the measured displacements are closer to the ground truth than the ones for 2 MMPs. Comparing (a) and (b) plots in Figure 13, Figure 14, and Figure 15, the proposed algorithm works very well to estimate the missing values in matrix $\mathbf{D}$. For the three cases discussed in this section, the dimensions of matrices $\mathbf{D}$ are 10×587, 10×497, and 10×407 with 2166, 1472, and 911 missing values, respectively. The corresponding missing rates for these three cases are 55.40%, 44.47%, and 33.61%. Figure 16 presents the errors of the matrix completion relative to the amplitude of the displacement at each VFP. We can see the error level is around 20%, and more MMPs lead to lower errors.
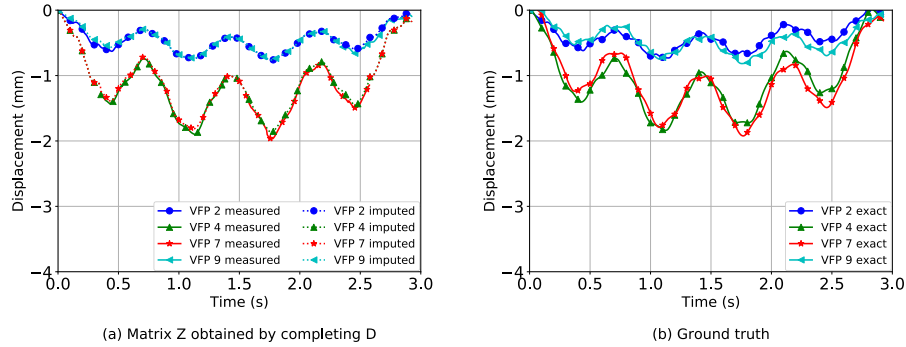

(a) Matrix Z obtained by completing D   (b) Ground truth

Figure 13 - Comparison between reconstructed displacements for 4 VFPs and ground truth (4 MMPs)

(a) Matrix Z obtained by completing D   (b) Ground truth
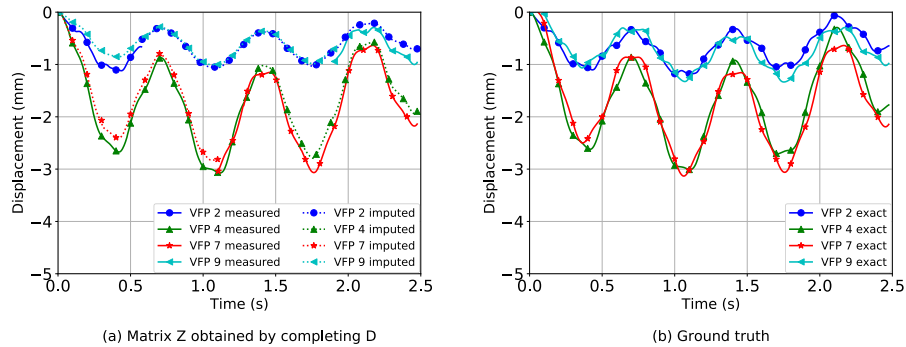
Figure 14 - Comparison between reconstructed displacements for 4 VFPs and ground truth (6 MMPs)

(a) Matrix Z obtained by completing D
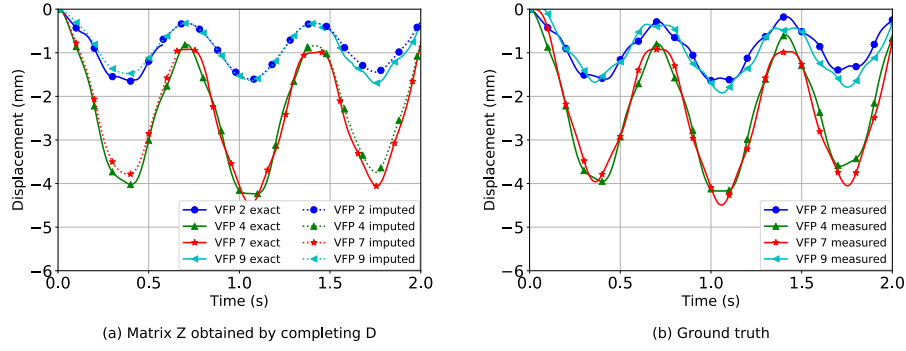
(b) Ground truth

Figure 15 - Comparison between reconstructed displacements for 4 VFPs and ground truth (8 MMPs)

(a) 4 MMPs

(b) 6 MMPs

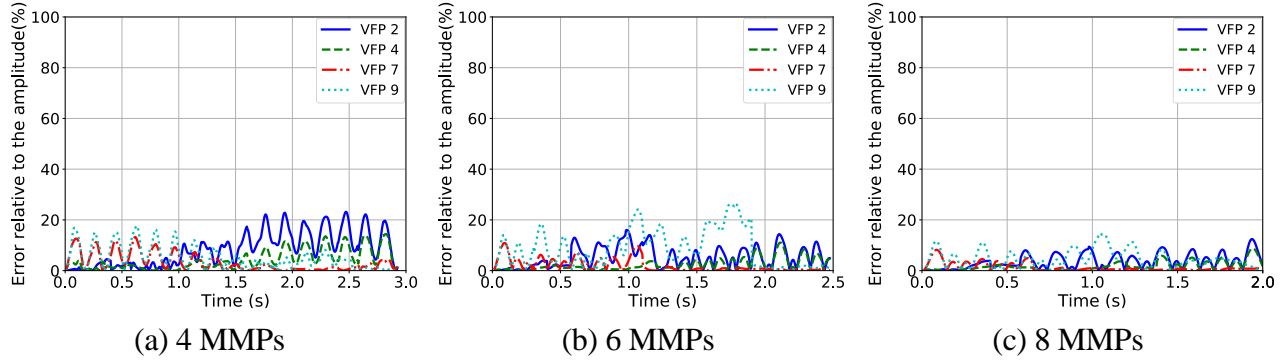(c) 8 MMPs

Figure 16 - Errors relative to the amplitude of each VFP

The first three mode shapes identified in these three cases are presented in Figure 17, and the MAC values for these modes are summarized in Table 2. Generally, all the modes are identified with a high accuracy in these three cases. The MAC values for second and thirds modes are all a little lower than the ones obtained by 2 MMPs, but the influence is not very significant. The possible reason for this phenomenon is that the mapping matrix $\mathbf{N_s}$ for 2 MMPs has lower dimensions and is more robust to the instability of pseudoinverse. The MAC values for the second mode decrease as more MMPs are used, but this is not the case for the third mode. Further investigation should be conducted to find more detailed relationships between the number of MMPs and MAC values.
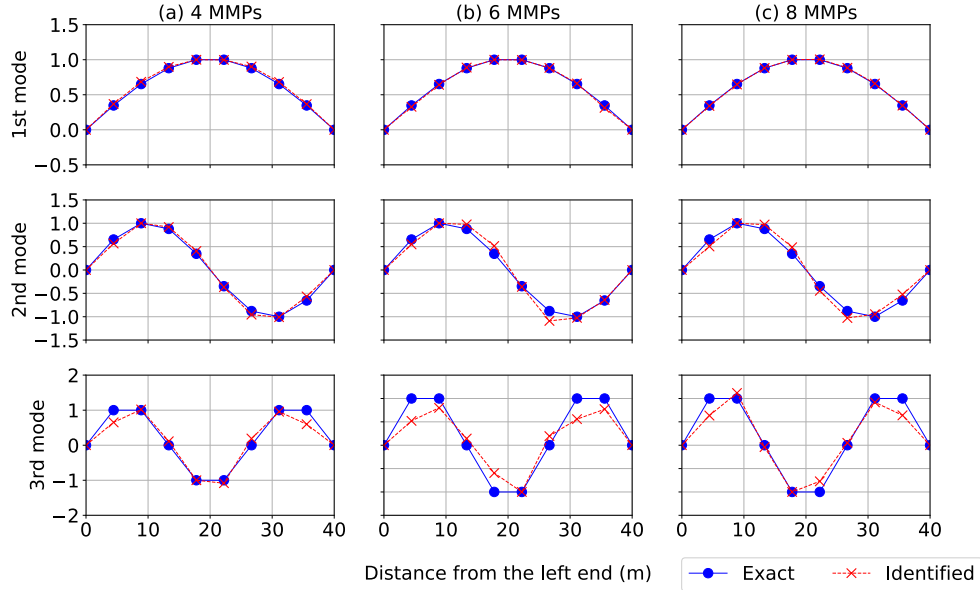
Figure 17 - The first 3 mode shapes identified from the proposed method

Table 2 – MAC values of the first 3 modes for 4, 6 and 8 MMPs

No. of MMPs	1st mode	2nd mode	3rd mode
4	1.000	0.994	0.947
6	1.000	0.986	0.930
8	1.000	0.979	0.956

4.2. Influence of car speed

The influence of the vehicle speed is discussed in this section. Figure 18 presents the MAC values for the first three modes at different speeds using 4, 6 and 8 MMPs. It is shown that the car speed has a very limited influence on the first mode since the MAC values for this mode are all around one for car speeds ranging from 10 to 80 km/h. The car speed has more influence on the second mode, and the most influence on the third mode. This makes sense since higher modes are less excited and harder to identify. From Figure 18(b), it is inferred that the MAC values of the second mode are around one, when the speed lies in the range of 20 to 60 km/h. Thus, it appears that moving either too slow or too fast can adversely affect the identification accuracy. From Figure 18(c), the MAC values of the third mode are higher for the speed range of 20 to 60 km/h for 2, 6 and 8 MMPs, but drop quickly starting at 50 km/h for the case of 4 MMPs. It should be also noted that the relationships of MAC values among 2, 4, 6 and 8 MMPs are different at different speeds. This also proves that not a sole factor is affecting the identification accuracy.

This section shows that unlike other mode shape identification methods as described in [23] where car speed has to stay at low levels, the proposed method can identify the first three modes very accurately even at nominal traffic speeds, which is a very important characteristic for real-life applications. The reason is that the matrix completion algorithm used in this paper is non-parametric,

and does not explicitly utilize the frequency domain information. Therefore, the accuracy of the system identification is not restricted by the Nyquist–Shannon sampling theorem [54].
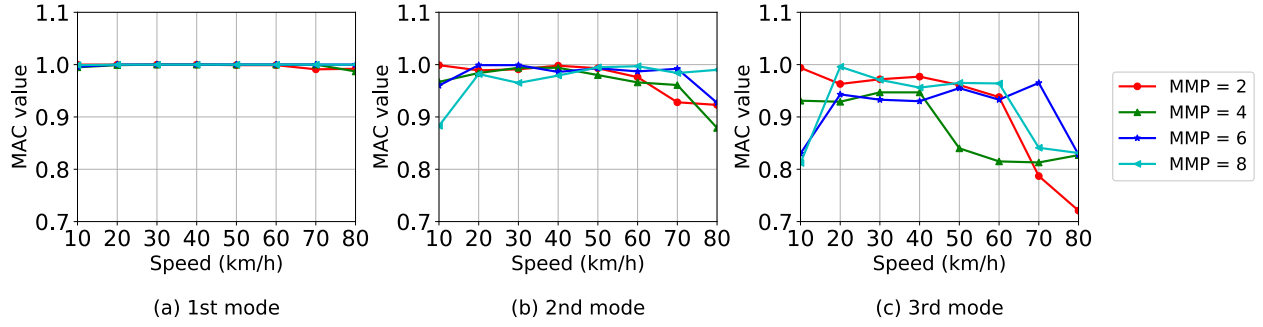

(a) 1st mode   (b) 2nd mode   (c) 3rd mode

Figure 18 – MAC values for the first three modes at different speeds
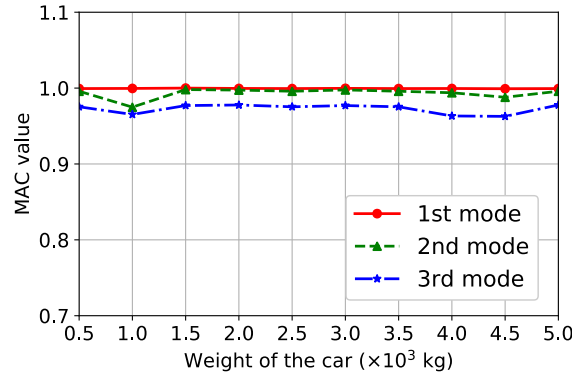
4.3. Influence of car weight

Figure 19 - MAC values for the first three modes for different car weights

Generally, the weight of a car varies from 1,000 kg to 3,000 kg [55]. This section discusses the influence of car weight on the mode shape identification. In this study, the car weights are simulated by assigning loads to MMPs. Considering the case of 2 MMPs, i.e., only one car, the weight of the car is evenly distributed to 2 MMPs where each MMP holds half weight of the car. Figure 19 shows the MAC values of the first 3 modes compared with ground truth by changing the car weight from 500 kg to 5,000 kg. It is seen that there is no significant decrease in MAC values when the car weight changes. In fact, according to the analysis, the MAC values do not change too much as long as the car weight is less than 1/10 of the bridge weight. This conclusion is consistent with Yang et al. [24]

4.4. Linear interpolation versus high-order Lagrange interpolation

The mapping step used in this paper was inspired by Oshima et al. [42] where they used high-order Lagrange interpolation to mapping displacements at MMPs to VFPs. Several issues are identified regarding applying high order Lagrange interpolation for the mapping which are listed below:

1) The number of MMPs has to be equal to the number of VFPs in order to calculate the inverse of their mapping matrices.

2) According to the observations, the inverse of their $\mathbf{N}(t)$ becomes very unstable when the MMPs are far from the given VFP.

3) The original study uses all the VFPs for the Lagrange interpolations which results in overfitting of the data and makes the mapping very sensitive to the noise and the locations of the MMPs. It was also acknowledged in [42] that the accuracy is lower when more MMPs are used.

To overcome the aforementioned issues, this paper proposes to use linear interpolation to replace high-order Lagrange interpolation, and limit the valid data to a range that is close to the MMPs. Also, Moore–Penrose inverse (i.e., pseudoinverse) is used instead of the standard inverse for the mapping. These improvements will make the inversion more stable while creating a sparse matrix. Then, a matrix completion algorithm follows to fill the sparse matrix.

In order to make a direct comparison between the proposed mapping method and the one used in [42], we set the number of VFPs to 10, including two VFPs at boundaries, and the number of MMPs to 8 as well even though our proposed method can use fewer MMPs. It should be noted that two VFPs at the boundaries are utilized by our proposed mapping method but not the one in Oshima et al. [42] The other parameters are the same as in §3.

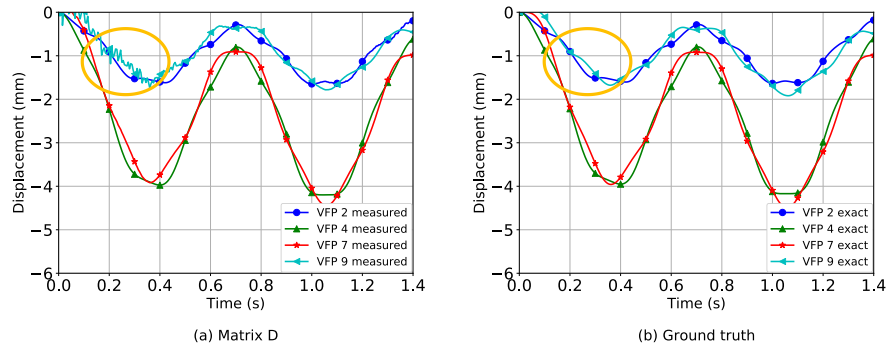
(a) Matrix D   (b) Ground truth

Figure 20 – Comparison between Lagrange mapping proposed in Oshima et al.[42] and ground truth

Figure 20 presents the comparison between the Lagrange mapping proposed in [42] and the ground truth for four VFPs. As seen in Figure 15, the proposed mapping can reconstruct the displacements at VFPs more accurately with missing values. However, the Lagrange mapping used in Figure 20 does not have missing values but have many inaccurate data points. For instance, as shown in the circled areas in Figure 20, the instability of the inverse results in some high frequency components which significantly reduces the performance of the system identification at higher modes.

The first three mode shapes identified from matrix $\mathbf{D}$ that is mapped by high order Lagrange interpolation are presented in Figure 21. The MAC values for these three modes are 1.000, 0.998 and 0.676. It is seen that the third mode is not identified correctly, which confirms that the instability of the mapping lead to inaccuracy in higher mode identification.

(a) First mode (a) Second mode (a) Third mode

Figure 21 - The first three normalized mode shapes identified from matrix **D** obtained by Lagrange mapping

4.5. Influence of regularization coefficient λ

In this section, the influence of the regularization coefficient λ is investigated. Using four MMPs as an example, different λ values ranging from 1 to 10^{-5} are used for the algorithm. The MAC values for the first three modes compared to the ground truth are presented in Figure 22. It is seen that the MAC values are small when λ is large. This is because if λ is too large, the regularization term of the objective function dominates the algorithm and masks the information of the mode shapes in the matrix. When λ becomes smaller, the MAC values of the first two modes reaches 1, but the MAC value of the third mode increases first and then decrease. This means lower modes are less sensitive to the regularization term, which makes sense because the regularization term aims to minimize the rank of the matrix. In practice, the error between valid elements within estimated matrix **Z** and matrix **D** and engineering judgement should be used to determine the optimal λ.
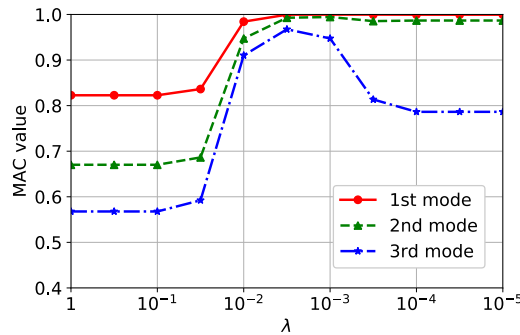

Figure 22 - MAC values for the first three modes for different regularization coefficient λ

4.6. Influence of Road Roughness

It is well accepted that one of the main challenges in indirect mode shape identification is the road roughness [23], which can dominate the recorded vibrations. In this method, road roughness is added to the simulation to examine the robustness of the proposed method. Following the power spectral density (PSD) based procedure given in Yang and Lee [56], three different road profiles are generated using $G_d(n_0)$ of 0.01×10^{-6} m^3, 1×10^{-6} m^3, and 16×10^{-6} m^3, representing low, medium and high road roughness, respectively. [56] The generated road profiles are presented in Figure 23.
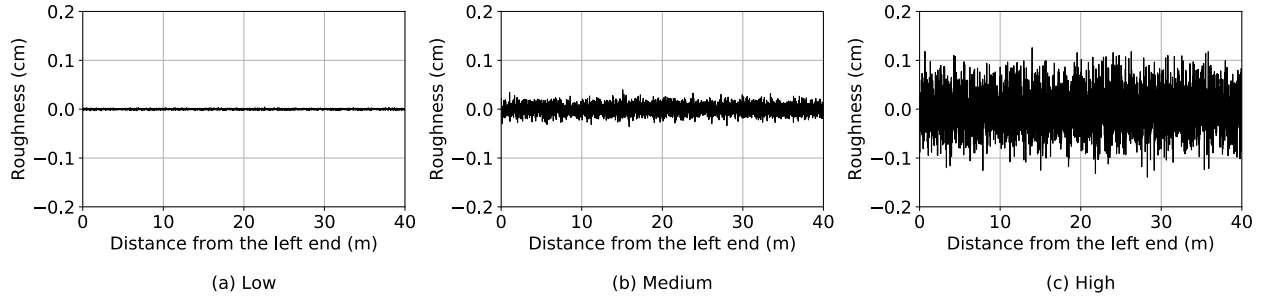
(a) Low   (b) Medium   (c) High

Figure 23 - Generated road roughness

The MAC values for these three road profiles are presented in Figure 24. It is demonstrated that for the low road roughness case, the MAC values for the first three modes are almost the same as the case without any roughness. As the road roughness increases, the MAC values decrease. The identification accuracy of the lower modes is more robust to the road roughness compared to higher modes. The MAC value for the first mode at high road roughness case is 0.876, while they are 0.750 and 0.492 for the second and third modes. It should be noted that the results in this section are obtained by directly applying the proposed method on rough road profiles. Preprocessing procedures like subtracting from two wheels [25, 42] or isolating the bridge vibration using blind source separation [47] could help reducing the effect of road roughness, but they are not studied in this paper.
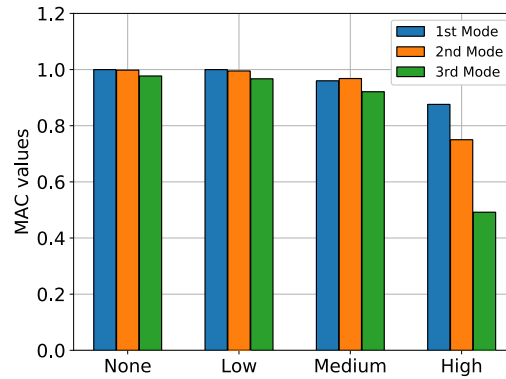

Figure 24 – MAC values for different road profiles

4.7. Influence of Noise

Except road roughness, the measurement errors could also play an important role in the performance of the proposed method. To investigate the influence of the measurement errors, artificial noise is added to all the acceleration data collected from the MMPs before calculating displacement data using integration. The noise is generated from a Gaussian distribution with the mean of 0 and the standard deviation as a percentage of the root mean square of the data. The noise levels from 0% to 5% are added in this study. The Signal-and-Ratios (SNR) for different levels are 40, 34, 31, 28 and 26 dB. Figure 25 presents the MAC values of different modes at different numbers of MMPs and noise levels. As expected, all MAC values decrease as the noise level increase. Among these three modes, the first one is least affected by the noise, and the third one is the most. Considering different numbers of

MMPs, the first and second modes identified using 8 MMPs are the most robust to the noise, but the MAC values of the third mode for 8 MMPs drop significantly as the noise level increases.
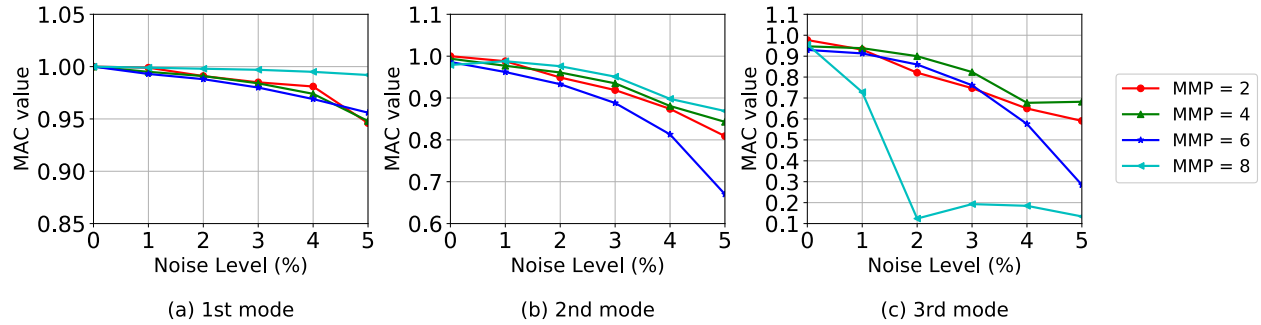

(a) 1st mode　　　　　　(b) 2nd mode　　　　　　(c) 3rd mode

Figure 25 – MAC values of the proposed method at different noise levels

5. Conclusions and Recommendations for Future Work

The paper presented a novel method for mode shape identification using data recorded on moving vehicles by converting it to a matrix completion problem. Linear interpolation is applied to map the data collected from vehicles to fixed VFPs on the bridge. Soft imputing algorithm is introduced to fill the missing values in the matrix due to the mapping. Numerical analyses are conducted to verify the method. The proposed method can use as few as one single vehicle to identify the first three modes with high accuracy. There are several advantages of this method compared to previous studies [25, 42]:

(i)　The method works at traffic speeds ranging from 10 to 60 km/h. These speeds are more practical, as compared to earlier methods, which only allows very low speeds.

(ii)　Through mobile scanning using the vehicle, the method can identify more modes with higher resolution, while using a much lower number of sensors than the fixed sensor scenario.

(iii)　The method does not explicitly use information from the frequency domain, and thus it is more robust to noise and measurement errors.

Despite promising results, it has to be acknowledged that more investigation should be conducted to further verify the method and to improve its capabilities—e.g., for considering multiple vehicles and automatically determining the optimal λ value. Experimental studies are planned also to validate the method.

Data Availability Statement

The data that support the findings of this study are available from the corresponding author upon reasonable request.

References

1.　Chourabi H, Nam T, Walker S, et al. Understanding Smart Cities: An Integrative Framework. 2012:2289-2297.

2.　Gomes EH, Dantas MA, Macedo DDD, Rolt CRD, Dias J, Foschini L. An infrastructure model for smart cities based on big data. *International Journal of Grid and Utility Computing*. 2018;9(4):322-332.

3.   Angelidou M, Psaltoglou A, Komninos N, Kakderi C, Tsarchopoulos P, Panori A. Enhancing sustainable urban development through smart city applications. *Journal of Science and Technology Policy Management*. 2018;9(2):146-169.

4.   Balaji AK, Soori PK. Sustainable Transportation Infrastructure for Smart Cities in the Gulf Cooperation Council: The Case of Electric Vehicle Charging. In: Samad WA, Azar E, eds. *Smart Cities in the Gulf: Current State, Opportunities, and Challenges*. Springer Singapore; 2019:107-121.

5.   Glancy DJ. Sharing the road: Smart transportation infrastructure. *Fordham Urb LJ*. 2013;41:1617.

6.   Xiong Z, Sheng H, Rong W, Cooper DE. Intelligent transportation systems for smart cities: a progress review. *Science China Information Sciences*. 2012/12/01 2012;55(12):2908-2914. doi:10.1007/s11432-012-4725-1

7.   Xiong Z, Cai Q, Liu F, Li L, Long Y. Dynamic performance of RAC-filled double-skin tubular columns subjected to cyclic axial compression. *Construction and Building Materials*. 2020;248:118665.

8.   Ham H, Kim TJ, Boyce D. Assessment of economic impacts from unexpected events with an interregional commodity flow and multimodal transportation network model. *Transportation Research Part A: Policy and Practice*. 2005;39(10):849-860.

9.   Mondoro A, Frangopol DM, Soliman M. Optimal risk-based management of coastal bridges vulnerable to hurricanes. *Journal of Infrastructure Systems*. 2016;23(3):04016046.

10.   Deng J, Dong W, Socher R, Li L-J, Li K, Fei-Fei L. Imagenet: A large-scale hierarchical image database. Ieee; 2009:248-255.

11.   Félio G. Informing the Future: The Canadian Infrastructure Report Card. Accessed October 18, 2019, http://canadianinfrastructure.ca/en/index.html

12.   Administration FH, Administration FT. *2015 Status of the Nation's Highways, Bridges, and Transit Conditions & Performance Report to Congress*. Government Printing Office; 2017.

13.   Wenzel H. *Health monitoring of bridges*. John Wiley & Sons; 2008.

14.   Ataei S, Nouri M, Kazemiashtiani V. Long-term monitoring of relative displacements at the keystone of a masonry arch bridge. *Structural Control and Health Monitoring*. 2018;25(4):e2144.

15.   An Y, Chatzi E, Sim SH, Laflamme S, Blachowski B, Ou J. Recent progress and future trends on damage identification methods for bridge structures. *Structural Control and Health Monitoring*. 2019;26(10):e2416.

16.   Ventura C, Kaya Y, Yao F, Huffmann S, Turek M. Seismic structural health monitoring of bridges in British Columbia, Canada. 2012:

17.   Guan S, Bridge JA, Li C, DeMello NJ. Smart radar sensor network for bridge displacement monitoring. *Journal of Bridge Engineering*. 2018;23(12):04018102.

18.   Mei Q, Gül M. Novel Sensor Clustering–Based Approach for Simultaneous Detection of Stiffness and Mass Changes Using Output-Only Data. *Journal of Structural Engineering*. 2014;141(10):04014237.

19.   Yang Y, Zhu Y, Wang LL, Jia BY, Jin R. Structural Damage Identification of Bridges from Passing Test Vehicles. *Sensors*. 2018;18(11):4035.

20.   Xu Y, Chen B, Ng C, Wong K, Chan W. Monitoring temperature effect on a long suspension bridge. *Structural Control and Health Monitoring*. 2010;17(6):632-653.

21.   Azim MR, Gül M. Damage detection of steel girder railway bridges utilizing operational vibration response. *Structural Control and Health Monitoring*. 2019;26(11):e2447.

22.   Mei Q, Gül M. A fixed-order time series model for damage detection and localization. *Journal of Civil Structural Health Monitoring*. 2016/11/01 2016;6(5):763-777. doi:10.1007/s13349-016-0196-1

23.   Malekjafarian A, McGetrick PJ, OBrien EJ. A review of indirect bridge monitoring using passing vehicles. *Shock and Vibration*. 2015;2015

24.   Yang YB, Lin CW, Yau JD. Extracting bridge frequencies from the dynamic response of a passing vehicle. *Journal of Sound and Vibration*. 5/6/ 2004;272(3–5):471-493. doi:http://dx.doi.org/10.1016/S0022-460X(03)00378-X

25.   Malekjafarian A, OBrien EJ. On the use of a passing vehicle for the estimation of bridge mode shapes. *Journal of Sound and Vibration*. 2017;397:77-91.

26.   Yang YB, Chang KC. Extraction of bridge frequencies from the dynamic response of a passing vehicle enhanced by the EMD technique. *Journal of Sound and Vibration*. 5/22/ 2009;322(4–5):718-739. doi:http://dx.doi.org/10.1016/j.jsv.2008.11.028

27.   Matarazzo TJ, Pakzad SN. Structural identification for mobile sensing with missing observations. *Journal of Engineering Mechanics*. 2016;142(5):04016021.

28.   Kim C-W, Chang K-C, McGetrick PJ, Inoue S, Hasegawa S. Utilizing moving vehicles as sensors for bridge condition screening—a laboratory verification. *Sensors and Materials*. 2017;29(2):153-163.

29.   Nayek R, Mukhopadhyay S, Narasimhan S. Mass normalized mode shape identification of bridge structures using a single actuator-sensor pair. *Structural Control and Health Monitoring*. 2018;25(11):e2244.

30.   Hester D, González A. A discussion on the merits and limitations of using drive-by monitoring to detect localised damage in a bridge. *Mechanical Systems and Signal Processing*. 2017/06/01/ 2017;90(Supplement C):234-253. doi:https://doi.org/10.1016/j.ymssp.2016.12.012

31.   Keenahan J, OBrien EJ, McGetrick PJ, Gonzalez A. The use of a dynamic truck–trailer drive-by system to monitor bridge damping. *Structural Health Monitoring*. 2014;13(2):143-157. doi:10.1177/1475921713513974

32.   Zhang B, Qian Y, Wu Y, Yang Y. An effective means for damage detection of bridges using the contact-point response of a moving test vehicle. *Journal of Sound and Vibration*. 2018;419:158-172.

33.   Zhu X, Law S-S, Huang L, Zhu S. Damage identification of supporting structures with a moving sensory system. *Journal of Sound and Vibration*. 2018;415:111-127.

34.   Sadeghi Eshkevari S, Pakzad SN, Takáč M, Matarazzo TJ. Modal identification of bridges using mobile sensors with sparse vibration data. *Journal of Engineering Mechanics*. 2020;146(4):04020011.

35.   Mei Q, Gül M, Boay M. Indirect health monitoring of bridges using Mel-frequency cepstral coefficients and principal component analysis. *Mechanical Systems and Signal Processing*. 2019/03/15/ 2019;119:523-546. doi:https://doi.org/10.1016/j.ymssp.2018.10.006

36.   Cantero D, McGetrick P, Kim C-W, Obrien E. Experimental monitoring of bridge frequency evolution during the passage of vehicles with different suspension properties. *Engineering Structures*. 2019/05/15/ 2019;187:209-219. doi:https://doi.org/10.1016/j.engstruct.2019.02.065

37.   Liu J, Chen S, Bergés M, et al. Diagnosis algorithms for indirect structural health monitoring of a bridge model via dimensionality reduction. *Mechanical Systems and Signal Processing*. 2020;136:106454.

38. Liu J, Bergés M, Bielak J, Garrett JH, Kovačević J, Noh HY. A damage localization and quantification algorithm for indirect structural health monitoring of bridges using multi-task learning. AIP Publishing LLC; 2019:090003.

39. Mei Q, Gül M. A crowdsourcing-based methodology using smartphones for bridge health monitoring. *Structural Health Monitoring*. 2018:1475921718815457.

40. Shirzad-Ghaleroudkhani N, Mei Q, Gül M. Frequency Identification of Bridges using Smartphones on Vehicles with Variable Features. *Journal of Bridge Engineering*. 2020;25(7):04020041.

41. Elhattab A, Uddin N, OBrien E. Drive-by bridge frequency identification under operational roadway speeds employing frequency independent underdamped pinning stochastic resonance (fi-upsr). *Sensors*. 2018;18(12):4207.

42. Oshima Y, Yamamoto K, Sugiura K. Damage assessment of a bridge based on mode shapes estimated by responses of passing vehicles. *Smart Structures and Systems*. 2014;13(5):731-753.

43. Malekjafarian A, OBrien EJ. Identification of bridge mode shapes using short time frequency domain decomposition of the responses measured in a passing vehicle. *Engineering Structures*. 2014;81:386-397.

44. OBrien EJ, Malekjafarian A. A mode shape-based damage detection approach using laser measurement from a vehicle crossing a simply supported bridge. *Structural Control and Health Monitoring*. 2016;23(10):1273-1286.

45. OBrien EJ, Malekjafarian A, González A. Application of empirical mode decomposition to drive-by bridge damage detection. *European Journal of Mechanics-A/Solids*. 2017;61:151-163.

46. Yang Y, Li Y, Chang K. Constructing the mode shapes of a bridge from a passing vehicle: a theoretical study. *Smart Structures and Systems*. 2014;13(5):797-819.

47. Eshkevari SS, Pakzad S. Bridge Structural Identification Using Moving Vehicle Acceleration Measurements. *Dynamics of Civil Structures, Volume 2*. Springer; 2019:251-261.

48. Eshkevari SS, Pakzad SN. Signal reconstruction from mobile sensors network using matrix completion approach. *Topics in Modal Analysis & Testing, Volume 8*. Springer; 2020:61-75.

49. Eshkevari SS, Takac M, Pakzad SN, Eshkevari SS. High resolution bridge mode shape identification via matrix completion approach. *Structural Health Monitoring 2019*. 2019;

50. Yang Y, Nagarajaiah S. Harnessing data structure for recovery of randomly missing structural vibration responses time history: Sparse representation versus low-rank structure. *Mechanical Systems and Signal Processing*. 2016/06/01/ 2016;74:165-182. doi:https://doi.org/10.1016/j.ymssp.2015.11.009

51. Nagarajaiah S, Yang Y. Modeling and harnessing sparse and low-rank data structure: a new paradigm for structural dynamics, identification, damage detection, and health monitoring. *Structural Control and Health Monitoring*. 2017;24(1):e1851.

52. Mazumder R, Hastie T, Tibshirani R. Spectral regularization algorithms for learning large incomplete matrices. *Journal of machine learning research*. 2010;11(Aug):2287-2322.

53. Jain P, Netrapalli P, Sanghavi S. Low-rank matrix completion using alternating minimization. 2013:665-674.

54. Oppenheim AV. *Discrete-time signal processing*. Pearson Education India; 1999.

55. Wikipedia. Gross vehicle weight rating. May 24, 2020, https://en.wikipedia.org/wiki/Gross_vehicle_weight_rating

56. Yang JP, Lee W-C. Damping effect of a passing vehicle for indirectly measuring bridge frequencies by EMD technique. *International Journal of Structural Stability and Dynamics*. 2018;18(01):1850008.